Scanning Microscopy Vol. 11, 1997 (Pages 31-42) 0891-7035/97$5.00+.25
Scanning Microscopy International, Chicago (AMF O'Hare), IL 60666 USA

QUANTIFICATION OF ENERGY FILTERED LATTICE IMAGES AND COHERENT CONVERGENT BEAM PATTERNS

C.B. Boothroyd

Department of Materials Science and Metallurgy, University of Cambridge, Cambridge, UK

Abstract

The extent to which energy filtered imaging allows quantitative matching of experimental and theoretical electron microscope images is investigated using two examples. In the first example, the matching of high resolution lattice images of $(WO_3)_8(Nb_2O_5)_9$, both energy filtered and unfiltered with a carbon surface layer, with corresponding simulations is considered. It is shown that in both cases even after all possible microscope and specimen parameters have been taken into account in the simulations, the contrast in lattice images obtained experimentally is only 1/3 of the contrast of corresponding simulated images. In the second example, energy filtered convergent beam patterns in a scanning transmission electron microscope are shown to depend sensitively on the microscope lens parameters and are used as a method of measuring defocus, spherical aberration and other microscope parameters.

Key Words: Energy filtering, coherent convergent beam patterns, quantification, lattice images, $(WO_3)_8(Nb_2O_5)_9$, inelastic scattering, lens aberrations.

*Address for correspondence:
C.B. Boothroyd
Department of Materials Science and Metallurgy, University of Cambridge,
Pembroke Street,
Cambridge CB2 3QZ, UK
Telephone number: +44 1223 334564
FAX number +44 1223 334567

Introduction

The quantitative comparison of experimental transmission electron microscope images with theory is an important goal that has always been difficult to realise. It is difficult to include inelastically scattered or "absorbed" electrons in image simulations and so the general procedure has been to arbitrarily scale the intensity and the contrast in the simulation to match the experimental image. The recent development of imaging filters coupled with charge-coupled device (CCD) detectors for image recording has meant that images can be filtered to separate the zero loss from the loss electrons for comparison with image simulations (Krivanek *et al.*, 1992). However, even for filtered images, a full quantitative comparison of experimental images with simulations is still not straightforward.

The purpose of this paper is to show the extent to which images and diffraction patterns can be analysed quantitatively with the aid of an imaging filter, and to this end two contrasting examples are given. Firstly I will give a brief summary of quantitative matching of high resolution images of $(WO_3)_8(Nb_2O_5)_9$. Only the major results are presented here, for more details see Boothroyd *et al.* (1995). The second example shows how lens aberrations can be determined from energy filtered coherent convergent beam patterns taken in a scanning transmission electron microscope.

Quantitative Matching of High Resolution Images and Simulations of $(WO_3)_8(Nb_2O_5)_9$

Typically, high resolution images are acquired unfiltered and are compared qualitatively with image simulations that have been calculated assuming only elastic scattering. Such comparisons are often poor when the images are compared quantitatively and good matches are generally only obtained because the imaging parameters and crystal thickness are left as free parameters to be determined during qualitative matching (Hÿtch and Stobbs, 1994). Boothroyd and Stobbs (1988, 1989) have shown that the effect of inelastic scattering on high resolution images is significant. Comparisons of the effects of inelastic scattering and carbon contamination on high resolution

Table 1. Percentages of the electrons lost from the incident beam for isolated $(WO_3)_8(Nb_2O_5)_9$ and carbon layers of the thicknesses analysed here.

	oxide	carbon
inelastically scattered	15%	15%
lost completely	11%	2%

images of $(WO_3)_8(Nb_2O_5)_9$ have also been made by Boothroyd *et al*. (1995). Here, I will summarise the major results concerning the matching of images and simulations of $(WO_3)_8(Nb_2O_5)_9$.

Images were obtained using a JEOL (Tokyo, Japan) 4000FX (C_s=~2°mm and C_c=1.4°mm) at 400°kV and a Gatan (Pleasanton, CA) imaging filter. The area examined consisted of a clean wedge-shaped crystal overlapping the edge of a carbon film, allowing the comparison of images of identical thickness with and without a carbon overlayer to model the effects of carbon contamination. All images were scaled so that the incident intensity when no specimen was present was unity. The words intensity and contrast have been used to mean different things in different papers. Here, to avoid confusion, I will use *intensity* to mean the average value in an image, *contrast* to mean some measure of the local variation in intensity (such as the standard deviation divided by the mean) and *pattern* to refer to the qualitative distribution of bright and dark dots in a lattice image.

About 8 unit cells of similar thicknesses from near the crystal edge were averaged to reduce noise from an elastic filtered image with no carbon and from an unfiltered image with a carbon layer, and are shown at the top of Figure 1 for a measured defocus of –74°nm. From these images, and similar elastic filtered images with carbon and unfiltered images without carbon, it is possible to deduce the fraction of the electrons inelastically scattered and lost completely ("absorbed") on passing through the thickness of $(WO_3)_8(Nb_2O_5)_9$ and carbon examined here. These values are shown in Table 1. The surprising result is that, even for the very thin region (~10°nm) of crystal examined, about 15% of the electrons have been inelastically scattered and when a carbon layer is also present this rises to 28% (i.e., (1 – (1–0.15)×(1–0.15))×100).

In order to produce simulated images all the necessary experimental parameters (e.g., defocus, energy spread, and beam divergence) were measured immediately after image acquisition, except for the crystal thickness which had to be estimated by comparison with simulations for different thicknesses. Although the thickness is a possible source of error, it was found that only a thickness of 10°nm

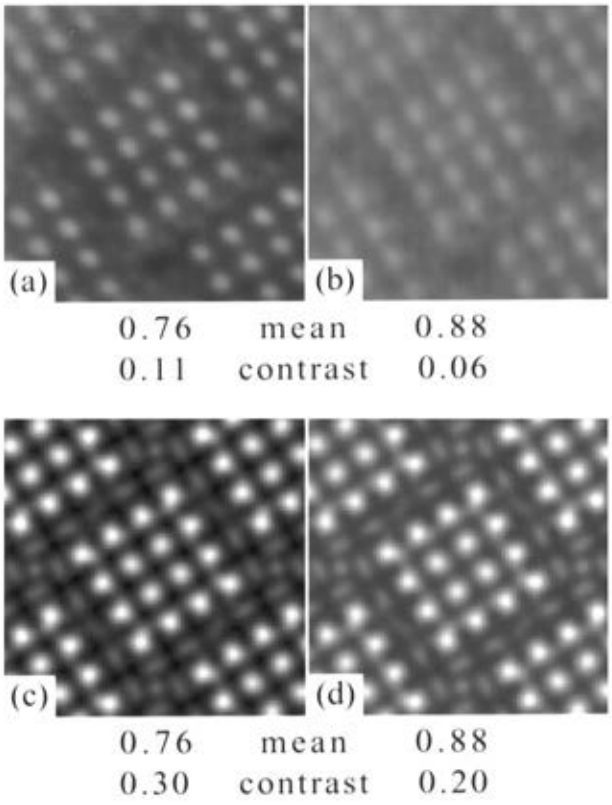

Figure 1. Comparison of energy filtered (left) and unfiltered (right), experimental (top row) and simulated (bottom row) lattice images of $(WO_3)_8(Nb_2O_5)_9$ for a defocus of –74°nm. The images were printed such that black corresponds to 0.5 and white to 1.4 on a scale where the incident intensity is 1. "Mean" is the average intensity in the image on this scale and "contrast" is given by the image standard deviation divided by the mean.

provided a good match to the *pattern* of the image. The method of simulating inelastic images is as described previously (Boothroyd *et al*., 1995; Boothroyd and Stobbs 1988, 1989). For the simulations of the unfiltered image with a carbon layer, the proportion of inelastic electrons included was that measured from the images and shown in Table 1, and their energy distribution was obtained from an energy loss spectrum acquired after the images from a similar area. The resulting simulations are shown at the bottom of Figure 1. The mean image intensity and its contrast, measured as the standard deviation divided by its mean is shown beneath each image. No attempt has been made to calculate from first principles the fraction of inelastic electrons for 10°nm of oxide. This fraction has been measured from the experimental images and hence the mean intensities for the simulations in Figure 1 agree with the experimental images. However, there is no agreement for the image contrast. In

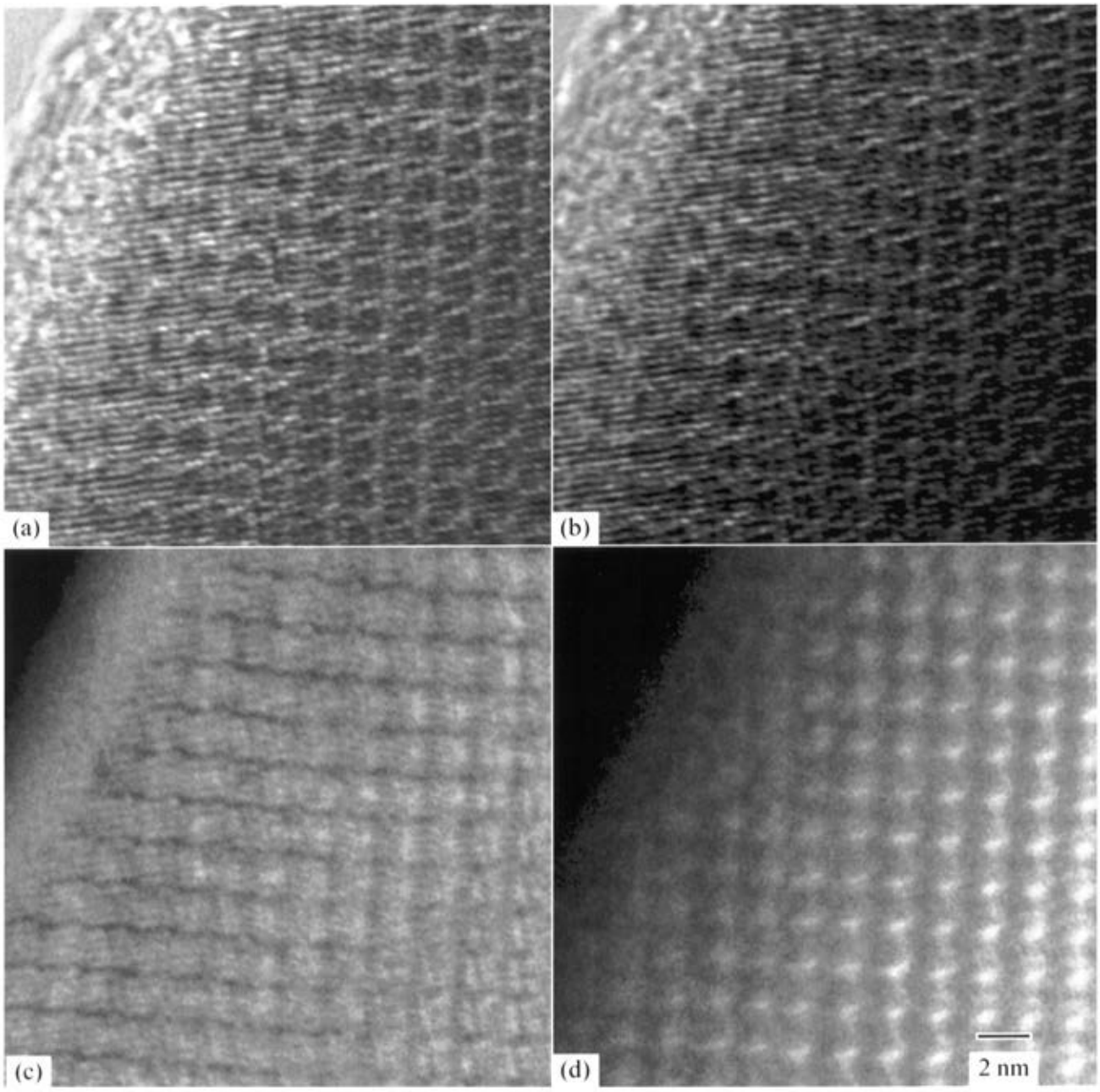

Figure 2. High resolution images of $(WO_3)_8(Nb_2O_5)_9$, (**a**) unfiltered, (**b**) zero loss filtered, (**c**) plasmon loss filtered, and (**d**) second plasmon loss filtered, taken using a Philips CM200 FEG at 200 kV. The intensities in (c) have been multiplied by 20 and (d) by 40 times.

both cases, the contrast in the experimental images is about 1/3 of that in the simulated images. A factor of 3 is a large disagreement and as I will show, there is no way of reducing it significantly. The beam divergence was measured from a selected area diffraction pattern. A specimen vibration amplitude of 0.05°nm was used in the simulations and it was found that larger values for the vibration, required to reduce the contrast to match the experimental images, removed too much high frequency detail before the contrast was reduced to the experimental level (the same would also apply to specimen drift). The focal spread, whose source is in the voltage and lens instabilities has, to first order, a similar effect on the image as vibration and thus could not be much larger than the value used, while an upper limit for

the voltage spread was in any case derived from the width of the zero loss peak in an energy loss spectrum. In this work, the effect of the point spread function of the detector was not included, but subsequent work has shown that under the conditions used here the contrast in the experimental images will have been reduced to no lower than 0.8 of its real value by the detector point spread function. Given that all these parameters have been measured accurately and none can be adjusted to reduce the contrast any more it is depressing that there is such a large discrepancy in the image contrast levels, especially given that intensities in diffraction patterns appear to have been calculated to greater accuracy (e.g., Saunders *et al*., 1995).

To end this section on a more optimistic note, recent images of the same oxide have been obtained on a Philips CM200 field emission gun (FEG) electron microscope (Philips Electron Optics, Eindhoven, The Netherlands) at 200kV (courtesy of Dr C.J.D. Hetherington and the National Center for Electron Microscopy, Lawrence Berkeley National Laboratory, Berkeley, CA) to assess the degree to which plasmon loss electrons do contribute contrast to a lattice image. Figure 2 shows unfiltered, zero loss filtered, first and second plasmon loss images of $(WO_3)_8(Nb_2O_5)_9$. The first plasmon loss image defocus was close to Scherzer defocus with the zero loss image being underfocus and the second plasmon loss image overfocus. The presence of lattice fringes in both the first and second plasmon loss images is clear and it will be interesting to determine whether the specimen thickness that most closely fits the plasmon loss images will be the same as that fitting the same area of the zero loss image. Figure 2 demonstrates that the methods used to include plasmon scattering in high resolution calculations are realistic.

Determination of Microscope Lens Parameters from Coherent Convergent Beam Patterns

The quantification of lattice images requires the fitting of image intensities to simulations and the last section has shown that this can be difficult. In this section I will give a preliminary description of how information can be obtained from energy filtered coherent convergent beam diffraction patterns. I will concentrate on the fringe positions, although the amplitude of the fringes depends on the spot size and coherence and in principle could provide a means of measuring these parameters (James *et al*., 1995).

It is well known in convergent beam electron diffraction that if the incident convergence angle is made larger than the Bragg angle for the diffraction maxima then the discs will overlap and interference may occur (e.g., Vincent *et al*., 1993). The criterion for interference fringes to be visible in the overlap region is that the spot size has to be small enough so that the image of the incoherent source when projected on the crystal is smaller than the plane spacing of the corresponding overlapping discs in the diffraction pattern. The spacing of the fringes produced depends on the probe defocus and can be thought of as a shadow image of the lattice planes. The fringes are straight for small incident convergence, but as the convergence is increased the spherical aberration of the probe forming lens becomes significant and the fringes are distorted into shapes that are dependent on the lens defocus. An example of the fringes formed as a function of defocus for a 111 GaAs systematic row collected using a Gatan imaging filter attached to a VG HB501 scanning transmission microscope (VG Microscopes, East Grinstead, UK) are shown in Figure 3. If the probe is overfocus (i.e., focused on a plane between the electron source and the specimen) then the fringes curve inwards at their ends (Fig. 3a). If the probe is well underfocus then the fringes curve outwards (Fig. 3d), and if the probe is only a little underfocus then more complicated patterns result (Figs. 3b, c). Given that these patterns consist mainly of bent fringes perpendicular to the $\mathbf{g}_{111}$ vector one might expect that the amplitude of their Fourier transform would contain a pair of fuzzy satellite spots whose distance from the center depended on the inverse of the fringe spacing. It is thus amusing that the patterns shown in Figure 4 for different probe defoci were discovered entirely by accident. Although the shape of the fringe patterns in the convergent beam pattern images changes considerably with defocus, their Fourier transforms always consist of two comet-shaped satellite spots whose position relative to the origin changes with defocus but whose shape, which resembles that of a spot affected by coma, remains constant.

Simulating Coherent Convergent Beam Patterns

As a first start towards understanding the origin of the fringes and the reason for the constant shape in the Fourier transforms, simulations of the patterns are required. A full simulation would involve calculating the phase shifts produced by the objective lens in the incident cone of electrons for the defocus required, and thus the shape of the probe on the specimen entrance surface, then propagating this electron distribution through the GaAs crystal using a multislice calculation. However, for thin specimens, as used here, it can be assumed that the diffracted beams are simply copies of the unscattered beam tilted by an angle corresponding to **g**. The diffracted beams have a different amplitude and are phase shifted by the crystal by an arbitrary constant amount with respect to the unscattered beam, but the change in amplitude only alters the amplitude of the resulting fringes and the crystal phase shift simply alters the phase of the fringes, leaving their spacings unchanged. Thus, a simple way of calculating the fringe positions in coherent convergent beam patterns is to

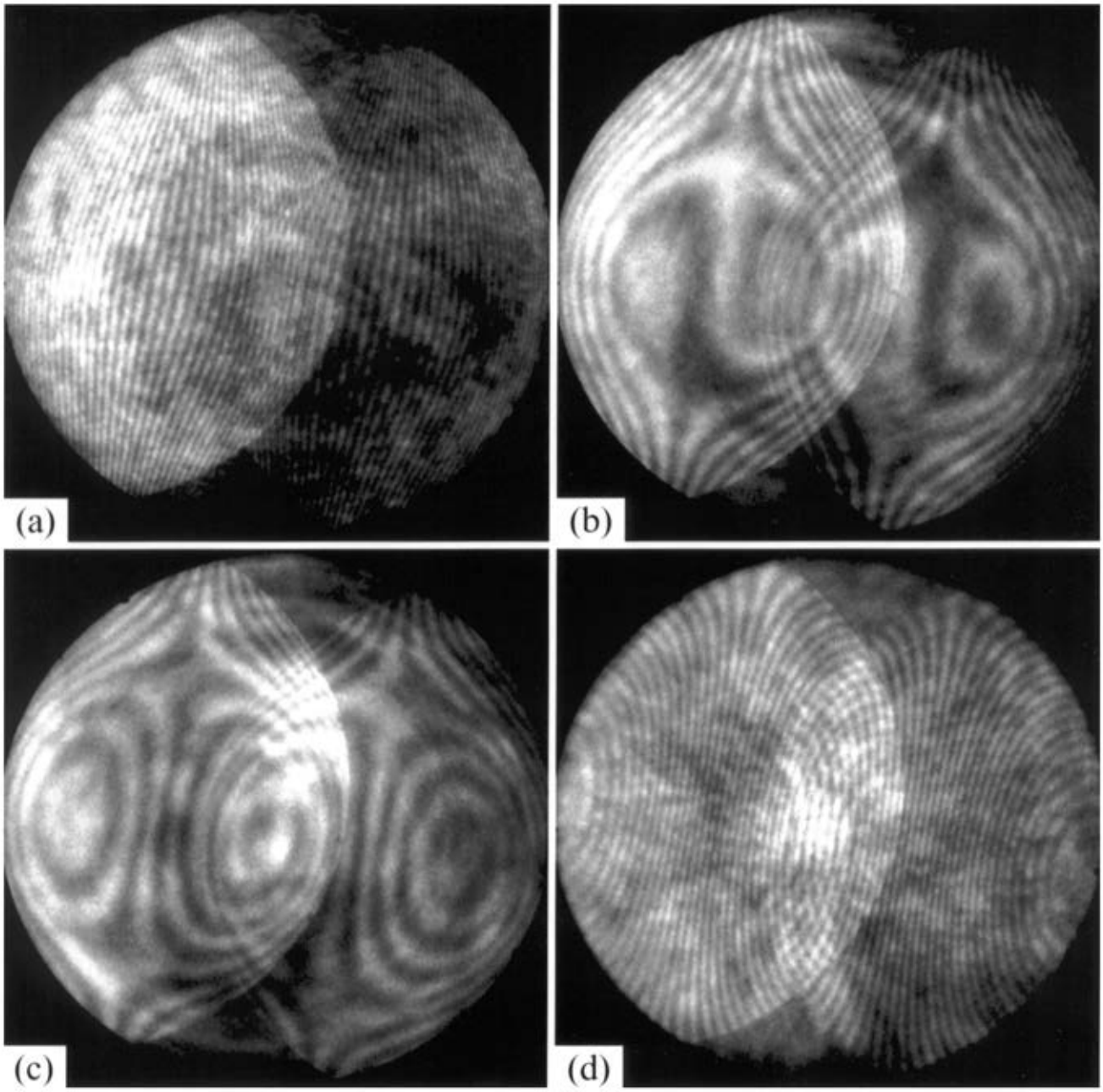

Figure 3. (**a-d**) Coherent convergent beam patterns from a 111 systematic row in GaAs with defocus changing from overfocus in (a) to underfocus in (d).

calculate the effect of the objective lens on the unscattered beam as a complex wave, then add copies of this with the same amplitude at angles corresponding to **g** and –**g** and calculate the modulus squared to get the intensity. The result of such a calculation for the conditions corresponding to Figure 3a, i.e., GaAs 111 with a defocus of 350°nm overfocus and a C_s of 3.1°mm, is shown in Figure 5a and its Fourier transform in Figure 5b. The fringe pattern of Figure 5a resembles closely that of Figure 3a and the comet-shaped satellite peaks of the Fourier transform are reproduced in Figure 5b. The first pair of comet-shaped peaks in Figure 5b away from the origin arises from the primary set of fringes in Figure 5a formed as a result of interference of the unscattered beam with the g and –g beams. These two peaks are crossed by fine straight fringes perpendicular to **g,** caused by the presence of the two identical sets of fringes in Figure 5a.

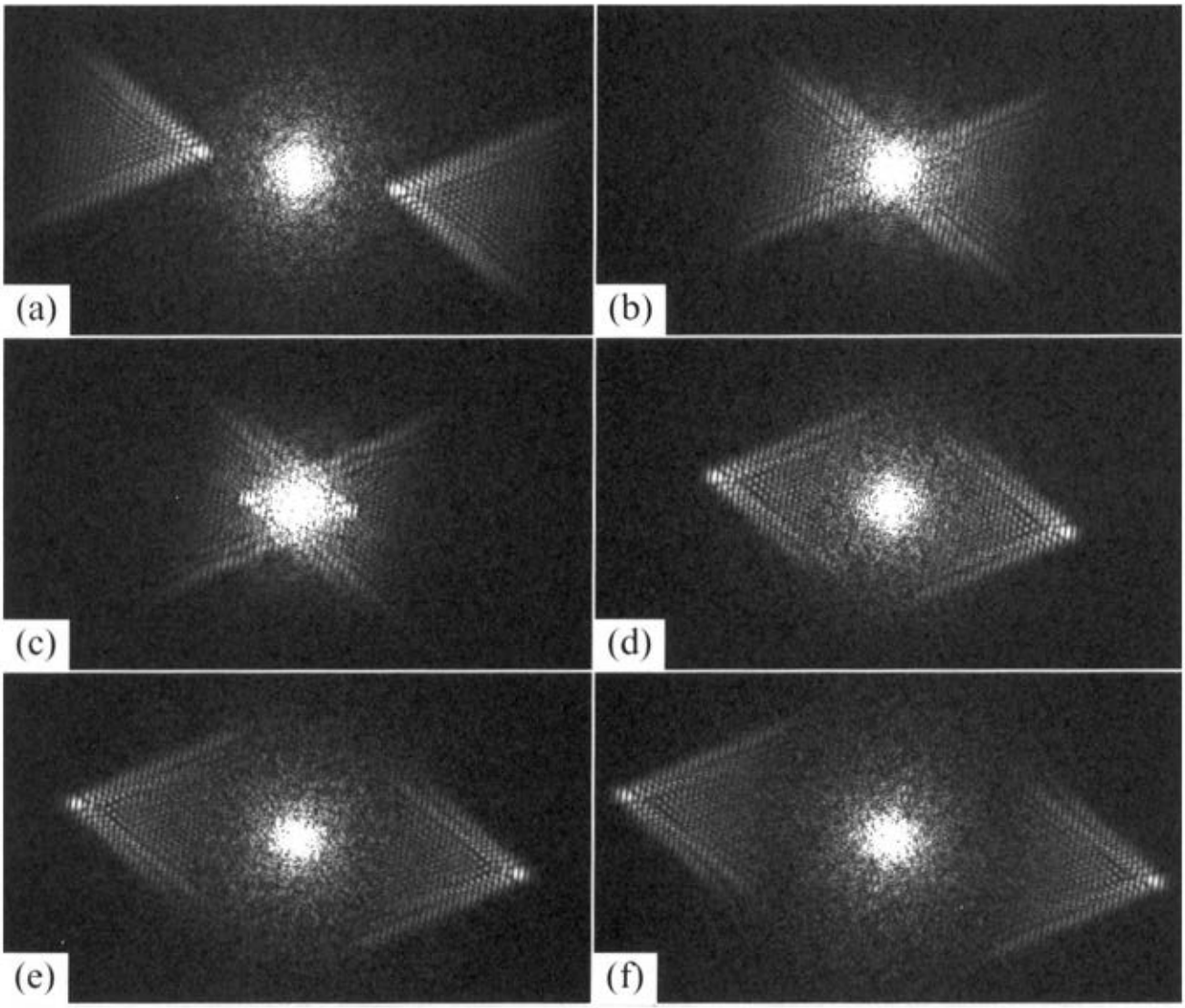

Figure 4. Amplitude of the Fourier transform of the convergent beam patterns in Figure 3. (**a**-**d**) correspond to Figure 3a-d whilst (**e**) and (**f**) are further underfocus.

These fine fringes are also visible experimentally in Figure 4. The pair of comet-shaped peaks furthest from the origin in Figure 5b arises from the interference fringes formed in the single small region of Figure 5a where the g and –g beams overlap and are thus not crossed by fine fringes. This second set of peaks is not seen in the Fourier transform of the experimental images (Figure 4), indicating that the microscope stability was not good enough for coherent interference between **g** and –**g**.

I have shown earlier how the Fourier transforms are affected by a change in the microscope defocus (Fig. 4) and it can be seen that the shape of the comet-shaped peaks remains unchanged and the comet's tail angle is always 60°. Next, I will discuss the effect of other microscope parameters on the coherent convergent beam fringes and their Fourier transforms. If no limiting objective aperture is used (Figs. 5c and 5d), then the comet-shaped peaks extend to much higher frequencies and 'wrap around' due to the

Figure 5 *(next three pages)*. (**a**) Coherent convergent beam simulation for a defocus of 350°nm, C_s of 3.1 mm and 100 kV corresponding to Figure 3a. (**b**) Fourier transform of (a). (**c**-**n**) As for (a) and (b) except (**c**) and (**d**) no objective aperture, (**e**) and (**f**) C_s = 10°mm, (**g**) and (**h**) astigmatism = 200°nm parallel to **g**, (**i**) and (**j**) astigmatism = 200°nm at 45° to **g**, (**k**) and (**l**) three-fold astigmatism = 2000°nm parallel to **g**, (**m**) and (**n**) three-fold astigmatism = 200°nm at 30° to **g**.

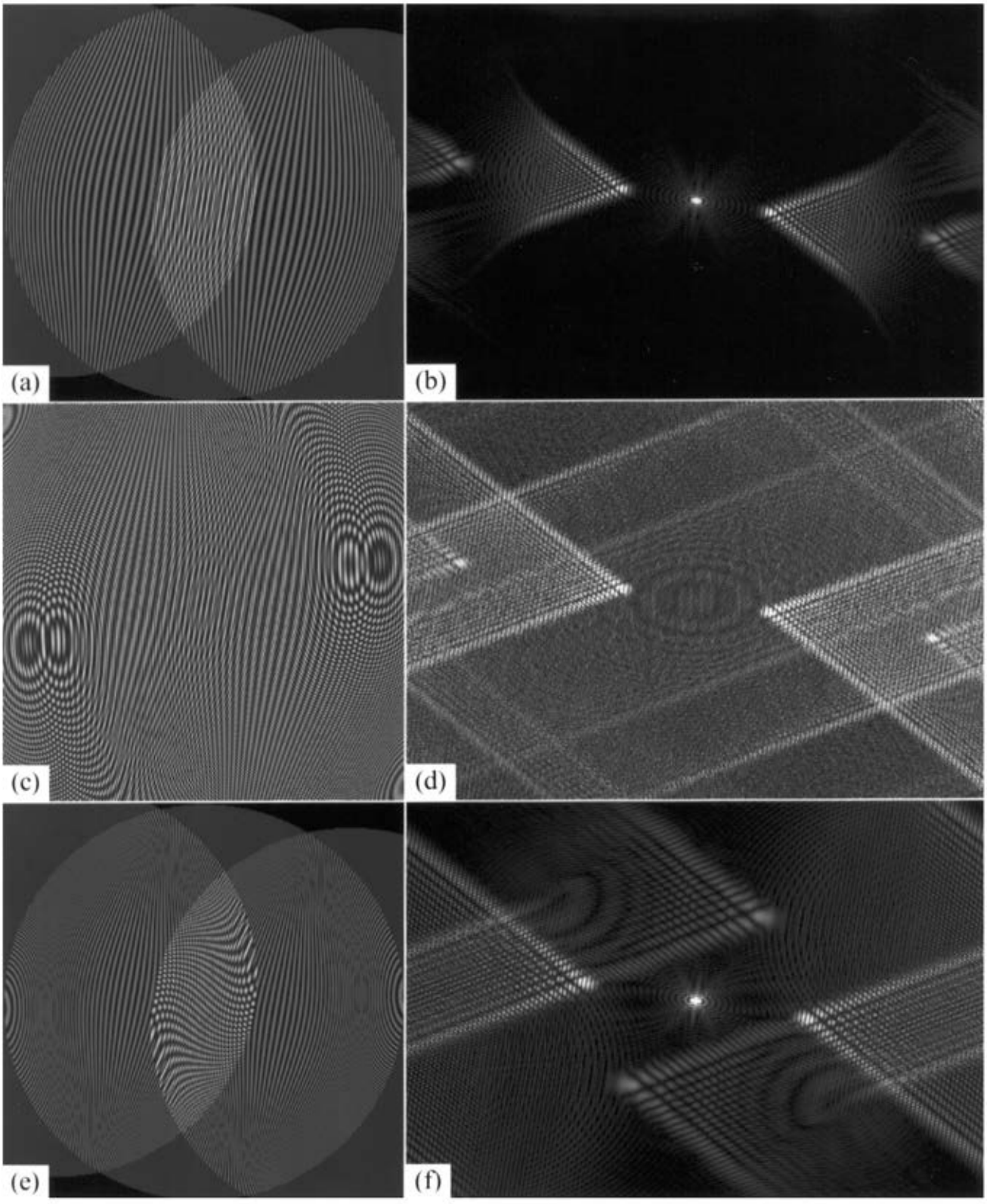
(a)
(b)
(c)
(d)
(e)
(f)

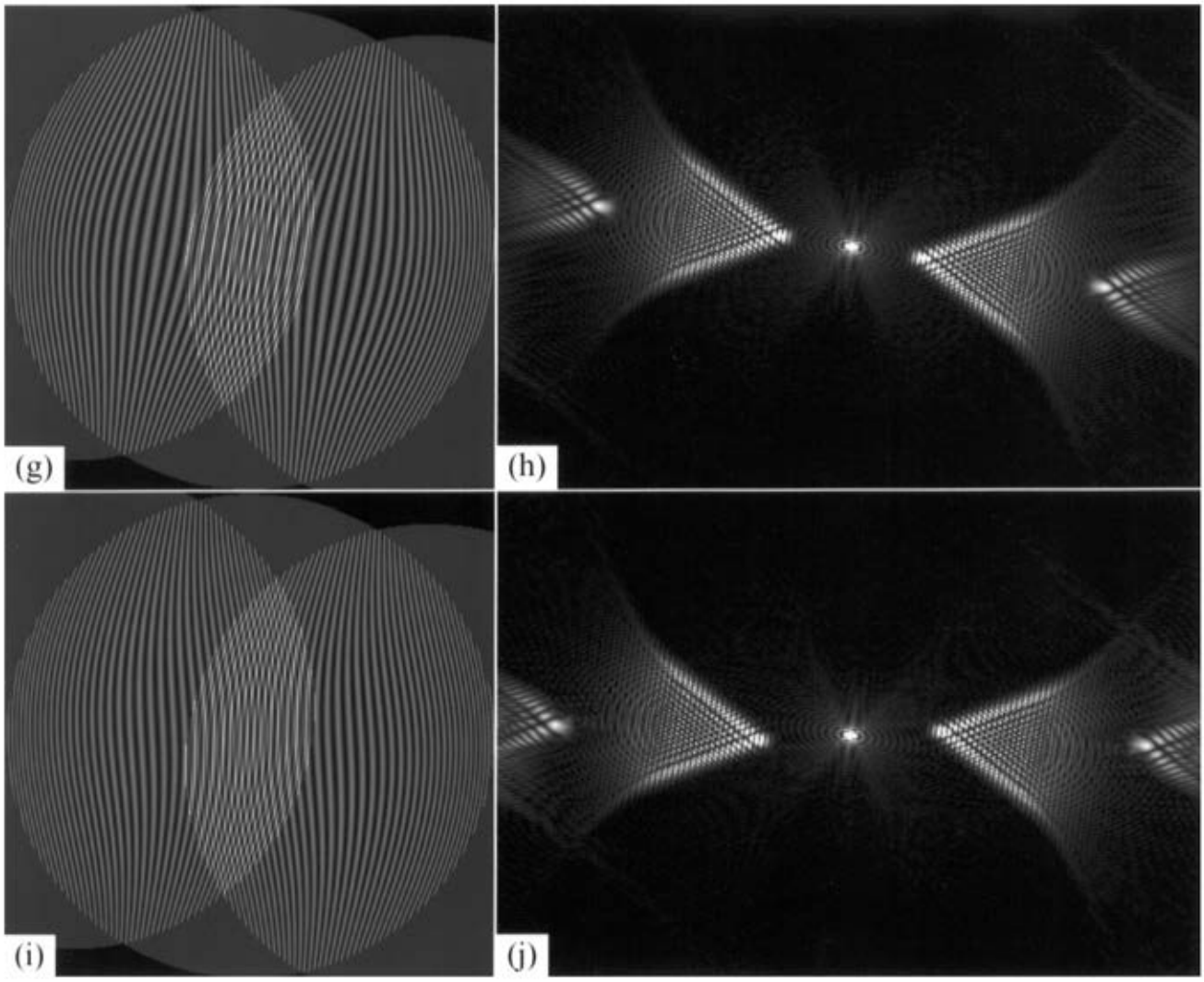

undersampling of Figure 5c. If the spherical aberration is reduced to zero, then not surprisingly the fringes become straight and the comet-shaped peaks lose their tails and are reduced to spots. For a larger C_s (Figs. 5e and 5f) the comet shape is again unchanged with the same 60° angle, but the comet's tail extends to higher frequencies. Figures 5g to 5j show the effect of 200°nm of astigmatism applied parallel to **g** (Figs. 5g and 5h) and at 45° to **g** (Figs. 5i and 5j). When the astigmatism is parallel to **g** (Figs. 5g and 5h), the effect is the same as if the defocus had been reduced by 200 nm, i.e., the fringe spacing is increased and the comet separation is decreased. For astigmatism applied at 45° to **g** (Figs. 5i and 5j) the fringes become 'S' shaped (including the central fringe in each pair of overlapping discs), and the comet-shaped peaks are displaced perpendicular to **g**, but again there is no change in the comet's shape. It can be seen that there is a little astigmatism present in the experimental Fourier transforms because of the asymmetry of the central fringe in Figure 3b and particularly in Figure 3c. Finally, if three-fold astigmatism is applied parallel to **g** (Figs. 5k and 5l), the fringes become more bent on one side of the central fringe in each pair of overlapping discs than the other and each peak splits into two comet-shaped peaks with different tail angles. For three-fold astigmatism applied at 30° to **g** (Figs. 5m and 5n), the fringes distort into an 'S' shape just as for two-fold astigmatism (Fig. 5i) but the central fringe in each pair of overlapping discs remains straight, and surprisingly there is very little change in the Fourier transform (Fig. 5n). Interestingly, the tails of the peaks in the experimental Fourier transforms in Figure 4 are split slightly into two tails with different angles, suggesting that three-fold astigmatism is present. This is especially noticeable in the underfocus images (Figs. 4i and 4j).

Quantifying coherent convergent beam fringe spacings

As shown in the last section and by Lin and Cowley (1986), the fringe positions contain information about the lens aberrations, although it is probably not possible to

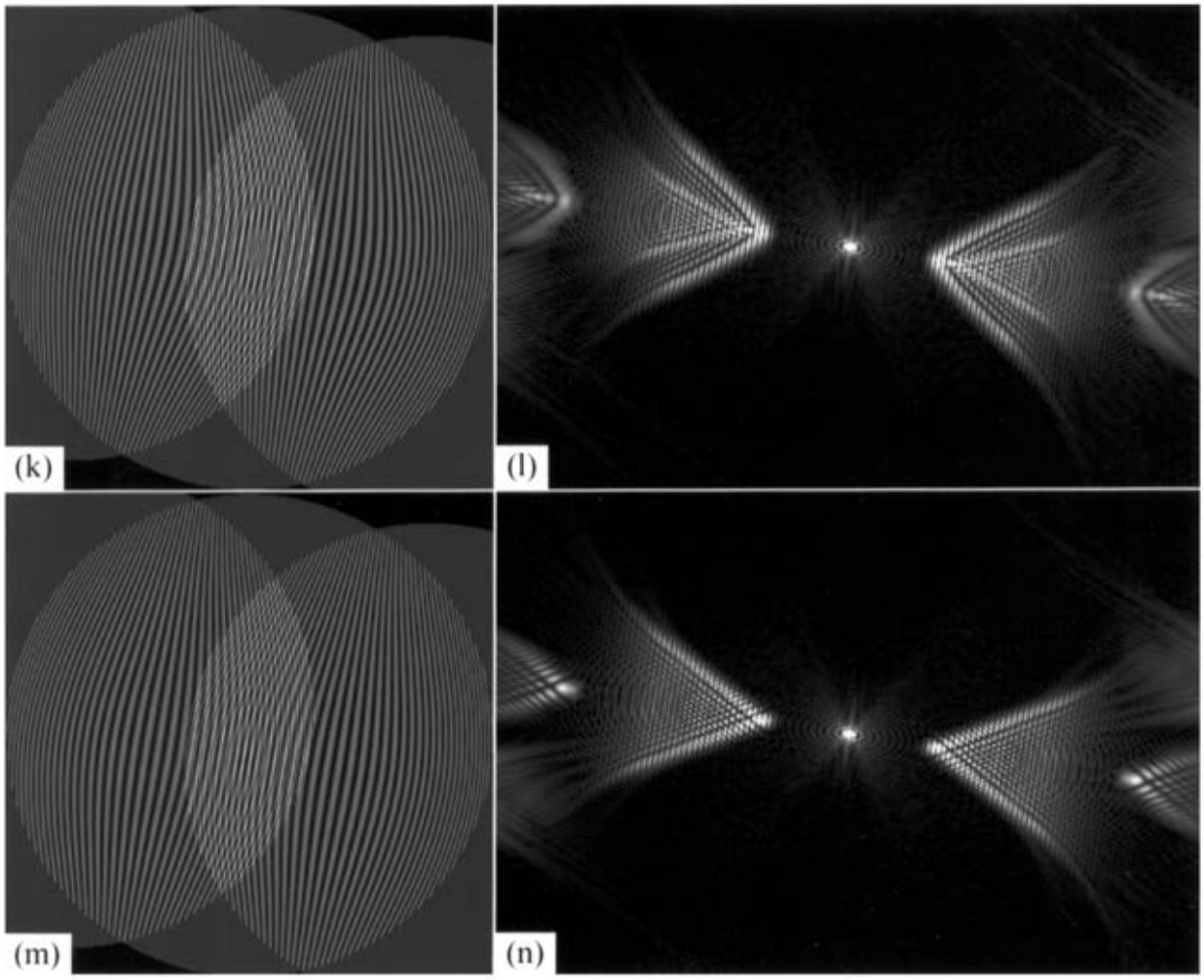

derive all of the lens parameters from just one pair of overlapping discs. In this section, I will attempt to show how the fringe positions can be measured from experimental convergent beam patterns and thus derive quantitative values for some lens parameters.

The fringes in a coherent convergent beam pattern can be treated like the fringes in a hologram in order to extract their amplitude and phase. The convergent beam pattern is Fourier transformed, a circular mask is drawn round one of the comet-shaped peaks and everywhere outside this mask is set to zero, then inverse Fourier transformed to give a complex image. The amplitude and phase of the complex image derived from Figure 3a are shown in Figures 6a and 6b. Moving the head of the comet-shaped peak to the center of the Fourier transform before inverse transforming simply removes a constant phase ramp and makes the phase look like that which would be obtained near zero defocus. This method will only work for large overfoci, and even larger underfoci, when the comet-shaped peaks in the Fourier transform are separated from the origin sufficiently to allow masking of one peak without including the origin or any part of the tail of the other peak.

In order to quantify the phase, I will consider a line through the unscattered 000 beam towards the g beam in a convergent beam pattern. The amplitude in the 000 disc will be constant up to the edge of the aperture then drop to zero, while the phase, ϕ_0, will be given by

$$\phi_0 = \pi\lambda^3 C_s k^4/2 + \pi\lambda d k^2 \qquad (1)$$

where λ is the electron wavelength, C_s the spherical aberration, d the defocus and k the reciprocal distance from the center of 000 towards g. The diffracted beam, g, will suffer a similar phase shift ϕ_g centered around $k^{\circ}=^{\circ}g$, plus the phase change introduced by the crystal, ϕ_{g0}. The resulting phase difference $\Delta\phi$ between the two beams will be

$$\Delta\phi = \pi\lambda^3 C_s/2\,(-4gk^3+6g^2k^2-4g^3k+g^4) + \pi\lambda d(-2gk+g^2) + \phi_{g0} \qquad (2)$$

In principle it should be possible to fit the phase from Figure

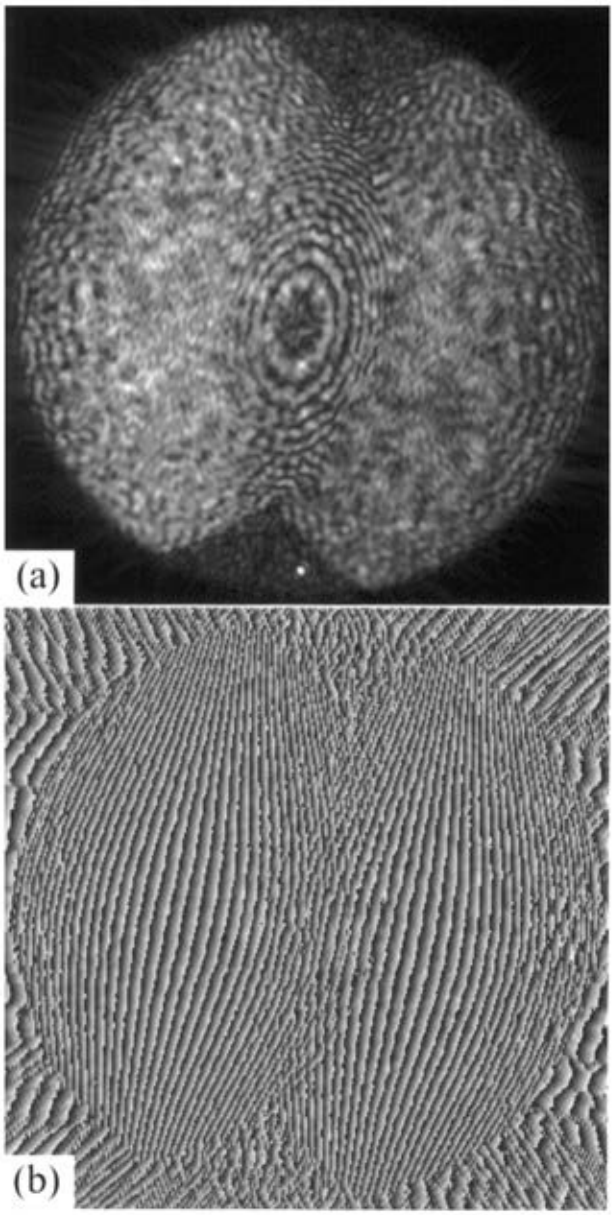

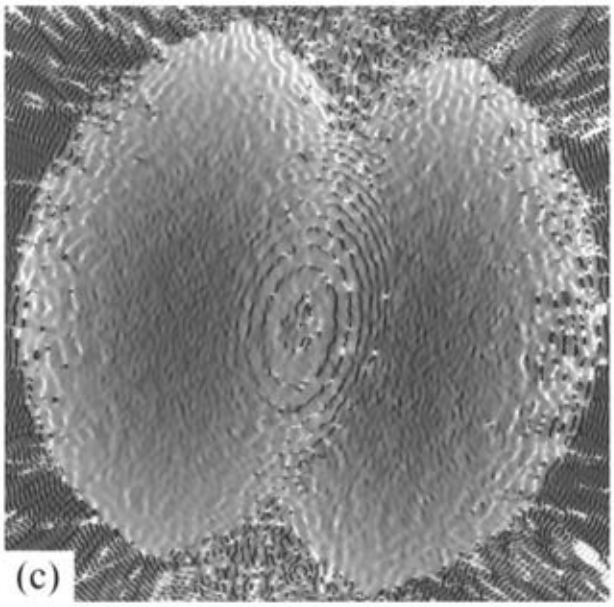

Figure 6. (**a**) Amplitude and (**b**) phase of the fringes derived from Figure 3a by masking one comet-shaped peak in the Fourier transform. (**c**) Phase differentiated along **g**.

6b to the above equation and so derive C_s, d and ϕ_{g0}. However, this is a messy process due to discontinuities in the phase. Fitting the differential of the phase was found to be a better way, viz:

$$d\Delta\phi/dk = 2\pi\lambda\gamma(-3\lambda^2C_sk^2+3\lambda^2C_sgk-\lambda^2C_sg^2-d) \qquad (3)$$

which depends only on C_s and d, and does not suffer from phase discontinuities.

$d\Delta\upsilon/dk$ for the experimental images should be calculated directly from the complex image to avoid phase discontinuities and is shown in Figure 6c. It is now possible to extract a strip from Figure 6c along the line joining 000 and g and derive C_s and d by least squares fitting to the equation for dDf/dk to give the values shown in Table 2. The values of C_s are all generally lower than the manufacturer's value of 3.1 mm for the lens and there is a large spread in the measurements. The figures from the underfocus values closest to focus are the least reliable, as a small part of the tail of the peak in the Fourier transform is cut off in the masking process because it lies too close to the origin. Nevertheless, it is exceptional that it is possible to measure any value for C_s and it must be remembered that only a small fraction of the available data are being used here. To make use of the full area of the disc overlaps in Figure 6c requires $d\Delta\phi/dk$ in 2 dimensions and as a function of astigmatism and three-fold astigmatism.

In conclusion, coherent convergent beam patterns provide a useful means of quantifying a microscope's spherical aberrations coefficient and defocus, while energy filtering is essential for the fine fringes to be visible.

Conclusions

I have shown how the intensity and contrast in energy filtered lattice images can now be compared quantitatively with image simulations. Unfortunately, such comparisons have shown that the experimental lattice image contrast is still about 3 times lower than that from the best fitting simulated images. This discrepancy needs to be understood before it is possible to match image patterns quantitatively. I have also shown that energy filtered

Table 2. Values of spherical aberration coefficient, C_s and defocus, d (underfocus negative), derived from dΔf/dk on the central line through 000 and g of the convergent beam patterns

d (nm)	C_s (mm)
360	2.5
90	2.5
-890	3.3
–1090	3.6
–1290	2.6

coherent convergent beam patterns provide a way of measuring the defocus, spherical aberration and astigmatism of the probe forming lens from their fringe positions. It is anticipated that their fringe intensities will enable the probe size and coherence to be measured.

Acknowledgements

I am grateful to Dr W.O. Saxton, Dr J.M. Rodenburg (who independently noticed the comet-shaped peaks), Dr R.E. Dunin-Borkowski and Dr W.M. Stobbs for useful discussions.

References

Boothroyd CB, Stobbs WM (1988) The contribution of inelastically scattered electrons to high resolution images of (Al,Ga)As/GaAs heterostructures. Ultramicroscopy **26**: 361–376.

Boothroyd CB, Stobbs WM (1989) The contribution of inelastically scattered electrons to [110] high resolution images of GaAs/AlAs heterostructures. Ultramicroscopy **31**: 259–274.

Boothroyd CB, Dunin-Borkowski RE, Stobbs WM, Humphreys CJ (1995) Quantifying the effects of amorphous layers on image contrast using energy filtered transmission electron microscopy. In: MRS Symposium Proceedings. Jacobson DC, Luzzi DE, Heinz TF, Iwaki M (eds). Materials Research Society, Pittsburg, PA. **354**: 495–500.

Hÿtch MJ, Stobbs WM (1994) Quantitative comparison of high-resolution TEM images with image simulations. Ultramicroscopy **53**: 191–203.

James EM, McCallum BC, Rodenburg JM (1995) Measurement and improvement of the effective source coherence in STEM. In: Institute of Physics Conference Series (Institute of Physics, Bristol, UK), **147**: 277–280.

Krivanek OL, Gubbens AJ, Dellby N, Meyer CE (1992) Design and first applications of a post-column imaging filter. Microscopy, Microanal Microstruct **3**: 187–199.

Lin JA, Cowley JM (1986) Calibration of the operating parameters for an HB5 STEM instrument. Ultramicroscopy **19**: 31–42.

Saunders M, Bird DM, Zaluzec NJ, Burgess WG, Preston AR, Humphreys CJ (1995) Measurement of low-order structure factors for silicon from zone-axis CBED patterns. Ultramicroscopy **60**: 311–323

Vincent R, Midgley PA, Spellward P (1993) Advances in coherent electron diffraction. In: Electron Microscopy and Analysis 1993. Institute of Physics Conference Series (Institute of Physics, Bristol, UK) **138**: 119–124.

Discussion with Reviewers

M. Saunders: Your results indicate that similar problems in matching the experimental and calculated contrast are observed in both unfiltered and filtered images indicating that the problem is still present after the inclusion of the majority of inelastic scattering events. One conclusion that could be drawn from this result is that the problem relates to phonon scattering which would still be present in the filtered image. How possible is it that errors in the modelling of phonon scattering give rise to these contrast problems?
Author: The inelastic scattering included in the calculations is only that due to plasmon and secondary electron losses. Phonon scattering is normally treated in low resolution images by the use of imaginary parts of the potential which to a first approximation reduce the beam intensities as the specimen thickness increases, distributing this intensity between the diffracted beams where it is stopped by the objective aperture, thus reducing only the image intensity and not the contrast. For high resolution, account has to be taken of the contribution this scattered intensity makes to the image as it is now not prevented from reaching the image by the objective aperture. Given these difficulties phonon scattering was ignored in these calculations, and I would expect it to be partially (but not wholly) responsible for the contrast problems observed.

P.D. Nellist: Would the author like to speculate on the origin of the discrepancy between the contrast in the simulated and experimental images? Does it not really indicate that the model of inelastic scattering used in the simulations is not accurate enough?
Author: It is quite possible that the inelastic scattering model used is not accurate enough, but at least for plasmon scattering it seems to account for the additional loss of contrast between filtered and unfiltered images. I believe the origin of the discrepancy is not simple, but is a combination of many factors that are not taken into account

in simulations. More work is needed to determine what the discrepancy is.

J. Rodenburg: The fact that the comet-like features in the Fourier Transform of the interference patterns described in the second half of the paper always have edges at 60 degrees is interesting. I presume it must be the result of a simple geometric constraint. The Fourier Transform of the shadow image is the auto-correlation of, as a first approximation, the product of the probe and specimen functions. Presumably spherical aberration (and, I believe, higher order aberrations) induces rings of equal phase in the probe, such that the integral of the autocorrelation goes to zero outside the comet-like features. Does the author have any understanding why this necessarily results in the comet shape? - or is there a better way of formulating the problem?
Author: I have thought about this problem a lot, but have not yet come up with a simple explanation for the comet shape.
P.D. Nellist: Measurements of the coefficient of spherical aberration using coherent convergent beam diffraction patterns has already been performed by Lin and Cowley (1986). How does the method of the author compare to their method, particularly with respect to their quoted accuracy (15%)?
Author: The method of Lin and Cowley (1986) requires a coherent convergent beam pattern where the objective aperture is large enough and the crystal aligned well enough so that the two diffracted beams are of the same intensity and all three beams overlap and interfere. This means that the lattice spacing of the crystal must be large enough (they used Beryl, lattice spacing 0.8°nm) to permit interference of the two diffracted beams with each other so that the ellipses that his method depends on are visible. For the material used here (GaAs 111, spacing 0.33°nm) this was not the case, and no ellipses are visible on Figure 3 although they are visible in the simulations of Figure 5. My method as described is less accurate than that of Lin and Cowley for determining C_s but it does work for the GaAs 111 discs shown and it's accuracy could be improved greatly by comparing the whole pattern rather than just the central row.